ACS APPLIED ELECTRONIC MATERIALS

pubs.acs.org/acsaelm Article

Effects of Crystalline Disorder on Interfacial and Magnetic Properties of Sputtered Topological Insulator/Ferromagnet Heterostructures

Nirjhar Bhattacharjee, Krishnamurthy Mahalingam, Adrian Fedorko, Alexandria Will-Cole, Jaehyeon Ryu, Michael Page, Michael McConney, Hui Fang, Don Heiman, and Nian Xiang Sun*

Cite This: *ACS Appl. Electron. Mater.* 2022, 4, 4288−4297 **Read Online**

ACCESS | Metrics & More | Article Recommendations | Supporting Information

ABSTRACT: Thin films of topological insulators (TIs) coupled with ferromagnets (FMs) are excellent candidates for energy-efficient spintronics devices. Here, the effect of the crystalline structural disorder of TI on the interfacial and magnetic properties of sputter-deposited TI/FM, $Bi_2Te_3/Ni_{80}Fe_{20}$, heterostructures is reported. Ni and a smaller amount of Fe from Py were found to diffuse across the interface and react with Bi_2Te_3. For improved crystalline *c*-axis-oriented Bi_2Te_3 films, a significant enhancement in Gilbert damping is observed, accompanied by an effective out-of-plane magnetic anisotropy and enhanced damping-like spin−orbit torque (DL-SOT), possibly due to the topological surface states (TSS) of Bi_2Te_3. Furthermore, a spontaneous exchange bias is observed in hysteresis loop measurements at low temperatures. This is caused by a topological antiferromagnetic interfacial layer formed due to a solid-state reaction between the diffused Ni with Bi_2Te_3 that couples with the FM, $Ni_{80}Fe_{20}$. For the increasing disorder of Bi_2Te_3, a significant weakening of the exchange interaction in the AFM interfacial layer is observed. These experimental results open the pathway for further exploration of crystalline-disordered TIs and their interfaces.

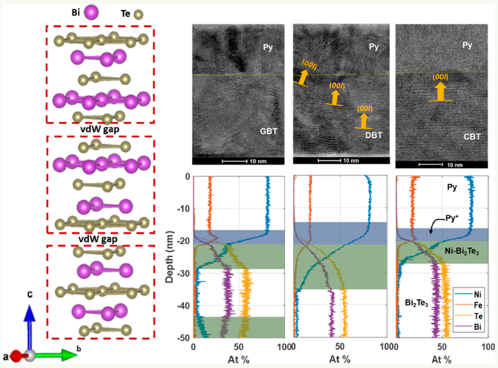

KEYWORDS: *Topological Insulator, Ferromagnet, Interface, Spin Pumping, Spin Orbit Torque, Antiferromagnet*

■ INTRODUCTION

Topological insulators (TIs) of the $(Bi,Sb)_2(Te,Se)_3$ family of compounds are van der Waals (vdW) chalcogenide materials with tetradymite structures. TIs possess large spin−orbit coupling (SOC) resulting in dissipation-less surface conducting states—topological surface states (TSS).[1−3] Introducing magnetic order in TIs leads to gap opening in the TSS bands and the possibility of dissipation-less quantum anomalous Hall (QAH) and axion insulator states.[4−21] Stimulated by these remarkable material properties, TIs are regarded as promising candidates for realization of energy efficient spintronic devices. TIs possess highly reactive surfaces, thus making them susceptible to the formation of interfacial phases when coupled with metallic films.[22−25] Because of their composition, these interfacial layers have the potential for hosting topologically nontrivial magnetic phases.[25] The majority of the reported experiments have studied TIs grown from molecular beam epitaxy (MBE),[22−24] which is a standard technique for growing high-quality, crystalline-ordered thin films. However, MBE suffers from low throughput and is constrained by sample dimensions, making it incompatible for integration in industrial CMOS processes. Magnetron sputtering, on the other hand, is the semiconductor industry's accepted thin film deposition technique because of its potential for high throughput and large area film growth. Sputtering also allows easy deposition of TIs with varying crystalline disorder.[25−29] This opens up the possibility of exploration of their disorder-dependent electronic and magnetic properties.

Recently, the topological antiferromagnetic (AFM) compound $NiBi_2Te_4$ was observed in the interface of highly *c*-axis-oriented sputtered $Bi_2Te_3/Ni_{80}Fe_{20}$ heterostructures.[25] Ni from the $Ni_{80}Fe_{20}$ (Py) layer diffuses and reacts with Bi_2Te_3, and the reaction is promoted by the delocalized TSS electrons.[23−25] In addition, recent experiments have shown the presence of Dirac-like surface states even in amorphous Bi_2Se_3.[30] In this work, the effects of crystalline structural disorder on the interface and magnetic properties of Bi_2Te_3/Py heterostructures are investigated. The magnetic species, largely Ni and smaller amounts of Fe, are found to diffuse across the interface into Bi_2Te_3, resulting in a magnetic interfacial layer. For increasing *c*-axis-oriented texture of Bi_2Te_3, increasing amounts of diffused magnetic species were found to react with Bi_2Te_3, which also leads to enhanced magnetic interactions at low

Received: April 21, 2022
Accepted: August 18, 2022
Published: August 31, 2022

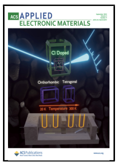

https://doi.org/10.1021/acsaelm.2c00523

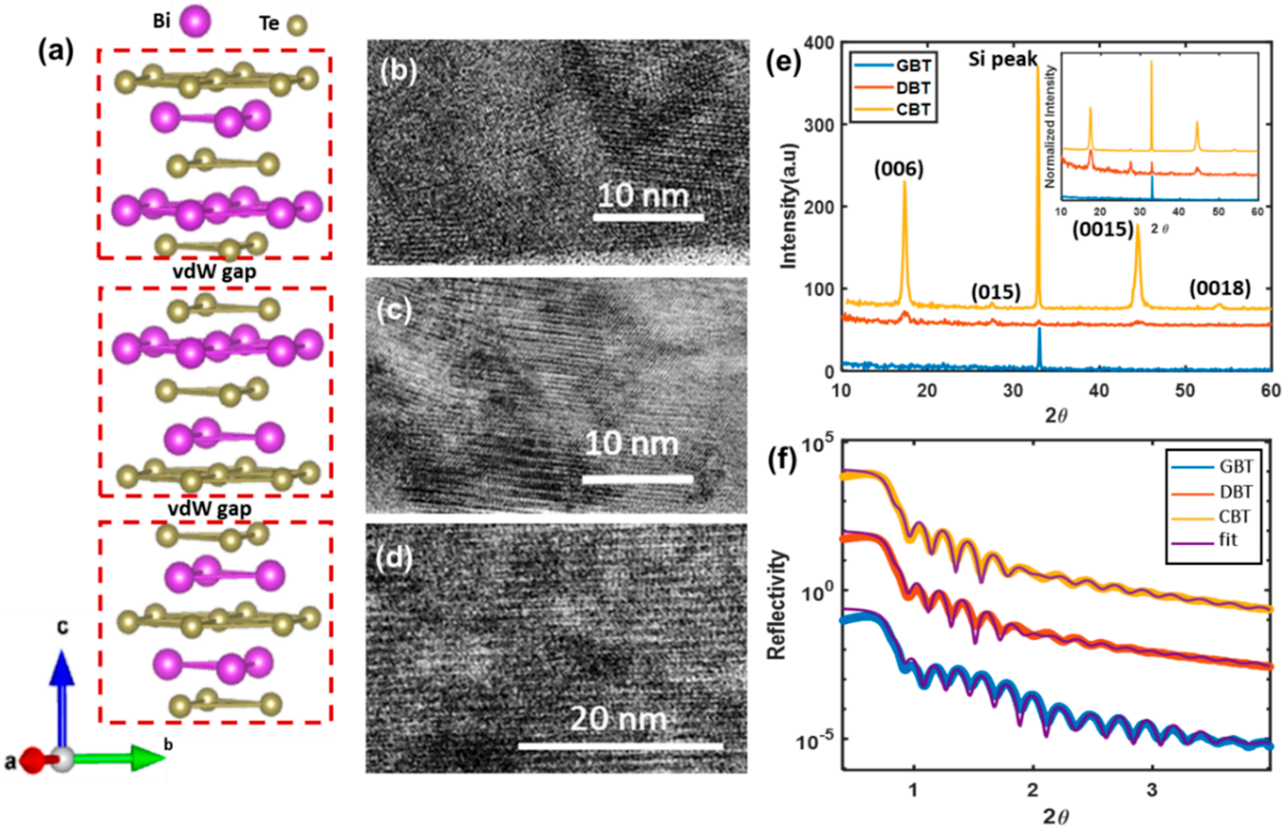

Figure 1. (a) Schematic model of three quintuple Bi_2Te_3 unit cells. Cross-sectional HRTEM images showing structural disorder in (b) GBT, (c) DBT, and (d) CBT samples. (e) XRD data for the GBT, DBT, and CBT samples. Inset: normalized plots of symmetric XRD data. (f) XRR plots and theoretical fitting for GBT, DBT, and CBT samples used for characterization of thickness and surface roughness. The data for CBT samples are similar to the ones in ref 25.

temperatures. This phenomenon was identified in hysteresis loop measurements of the magnetic moment versus applied magnetic field, $m(H)$, for the Bi_2Te_3/Py samples. As a result of the interfacially diffused magnetic species (Ni, Fe) reacting with Bi_2Te_3, the magnetic moment, m, at saturation field is reduced by Δm in the Bi_2Te_3/Py compared to control Py samples suggesting a change in valence state of the magnetic species. The values of Δm become smaller for increasing disorder in Bi_2Te_3, suggesting lesser reactivity between the diffused magnetic species and Bi_2Te_3. Further, a significant enhancement in Gilbert damping, an out-of-plane (OP) canting of magnetization, and enhanced DL-SOT were observed in samples with higher *c*-axis-oriented textured TI. However, with significantly reduced crystallinity, surprisingly the granular Bi_2Te_3 samples had a comparable enhanced spin-Hall conductivity as samples with the higher *c*-axis-oriented Bi_2Te_3. This can be attributed to the quantum confinement effect in smaller crystallite grains in granular TI.[26,27] Low-temperature $m(H)$ and $m(T)$ measurements revealed an AFM ordered phase in the predominantly Ni-diffused Bi_2Te_3 interface from the formation of the topological AFM compound $NiBi_2Te_4$.[25] Interestingly, the strength of the exchange interaction of the interfacial AFM phase, as monitored by the exchange bias, was found to weaken significantly with the increase in disorder of the Bi_2Te_3 layer. These results indicate a strong topological property of TIs with crystalline *c*-axis-oriented texture, which weakens considerably with increasing crystalline disorder. These experimental results show the possibility of tailoring topological properties of TIs by control of the crystalline structural disorder.

■ RESULTS AND DISCUSSION

Crystalline Structure−Properties of Sputter-Deposited Bi_2Te_3. Samples of ∼30 nm Bi_2Te_3 with varying crystalline disorder, (1) *granular* (GBT), (2) randomly oriented polycrystalline *disordered* (DBT), and (3) effectively *c*-axis-oriented *crystalline* (CBT), were grown using RF magnetron sputtering on amorphous thermally oxidized Si substrates (see FMR Measurements for material growth method and Supporting Information Section S1 for grain size characterization). The choice of amorphous thermally oxidized SiO_2 substrates was to decouple Si lattice effects for disordered TI samples. Crystalline structural properties of the Bi_2Te_3 samples were verified using X-ray diffraction (XRD) and high-resolution transmission electron microscope (HRTEM) imaging measurements, as shown in Figure 1a,b,d. The GBT samples did not show any significant diffraction peaks in the XRD measurement, suggesting a high amorphous content. Further, HRTEM images of the GBT, DBT, and CBT samples shown in Figure 1a verifies the granular, randomly oriented crystallite domains and an improved *c*-axis-oriented vdW layered structure, respectively. The thickness and surface roughness of the samples were characterized using X-ray reflectometry (XRR) measurements, as shown in Figure 1e. From the fitting of XRR data, thickness of ∼30 nm was obtained for all three samples. The fits to the XRR data also revealed surface roughness of 0.7, 1.7, and 1.0

nm for the GBT, DBT, and CBT samples, respectively, which are typical surface roughness values for sputter-deposited thin films, confirming growth of high-quality TI films. The XRR measurements also reveal densities of 9.06 g/cm^3, 9.47 g/cm^3, and 9.31 g/cm^3 for the GBT, DBT, and CBT samples, respectively. These values of density of Bi_2Te_3 are comparable and do not follow any noticeable trend.

Morphology of Interfacial Layer formed by Ni Diffusion into Bi_2Te_3. Heterostructure samples of GBT/Py, DBT/Py, and CBT/Py were grown where the thickness of the layers was maintained at 30 and 20 nm for Bi_2Te_3 and Py, respectively (see FMR Measurements for the material growth method). HRTEM imaging and energy dispersive X-ray spectroscopy (EDS) measurements were performed to characterize the morphology and stoichiometric composition along the cross section of the samples, as shown in Figure 2a−f (see Supporting Information Section S2). The HRTEM images in Figure 2a−c clearly show the highly amorphous nature of GBT, randomly oriented vdW layered crystalline domains in DBT, and highly oriented vdW layers in the CBT layers. A closer examination of the interfaces of the heterostructures also reveal a rougher interface in the disordered GBT/Py and DBT/Py samples compared to the CBT/Py sample. The EDS cross-sectional profiles of atomic % of elements in Figure 2d−f show a significant diffusion of Ni (and smaller amounts of Fe) across the TI/FM interface into the Bi_2Te_3 layers, forming an interfacial layer denoted as Ni−Bi_2Te_3. In general, the Ni and Fe show a large gradient over a Bi_2Te_3 distance of 5−14 nm, where the Ni averages 30−40%, while the Fe diffusion is much smaller in the GBT/Py and CBT/Py samples. The more highly disordered GBT/Py and DBT/Py samples also have ∼3% of Ni diffused throughout the thickness of the Bi_2Te_3 layer. However, the predominantly Ni−Bi_2Te_3 layer in the highly ordered CBT/Py sample acts as a barrier preventing further diffusion of Ni into the Bi_2Te_3 bulk. The formation of the Ni−Bi_2Te_3 layer is likewise accompanied by a thin Fe-enriched region in the intermediate Py layer (marked Py*). It must also be noted that the moderately disordered DBT/Py sample which has randomly oriented polycrystalline domains has developed a much higher Ni and Fe diffusion of ∼47% and ∼9% at the interface, respectively. The Fe diffusion, however, is only ∼3−4% at the interface in the GBT/Py and CBT/Py samples.

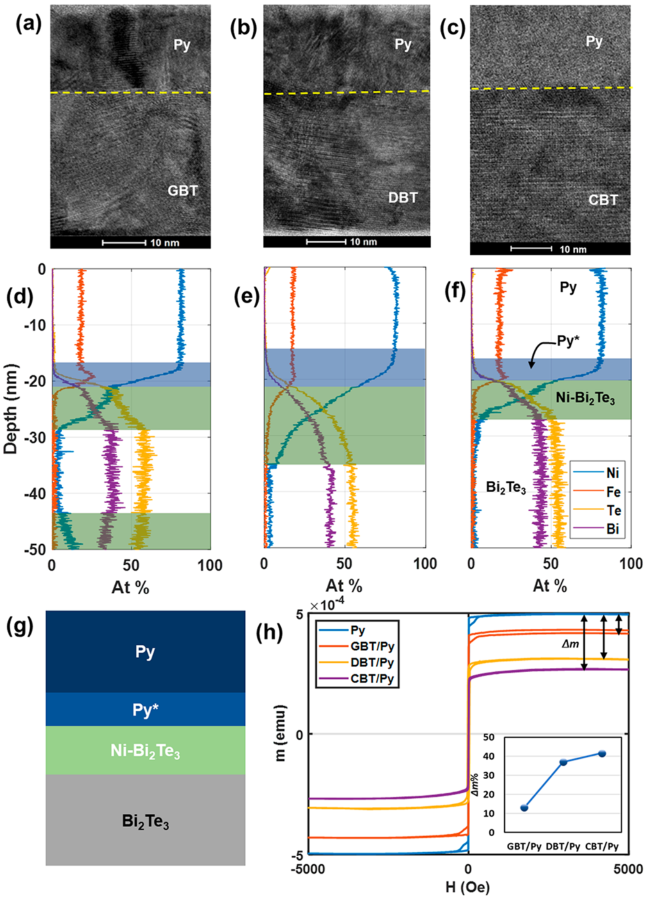

Figure 2. Cross-sectional HRTEM images of (a) highly amorphous GBT/Py, (b) disordered DBT/Py with randomly oriented vdW domains, and (c) highly *c*-axis-oriented CBT/Py (similar to ref 25). The yellow dashed lines mark the approximate boundary between the Bi_2Te_3 and Py layers without considering the interface layers. Atomic % (At %) characterized using EDS for (d) GBT/Py, (e) DBT/Py, and (f) CBT/Py samples. The interface layers are highlighted in green and blue colors for the Ni−Bi_2Te_3 and Py*, respectively. (g) Schematic of the Bi_2Te_3/Py samples with the layers marked. **h)** $m(H)$ measurements for IP orientation at room temperature showing loss of moments in the Bi_2Te_3/Py samples due to interfacial Ni and Fe diffusion and reaction with Bi_2Te_3. Inset: comparison of % loss of moments ($\Delta m\%$) in GBT/Py, DBT/Py, and CBT/Py samples compared to the control Py sample. The data presented for the CBT sample are similar to the ones in ref 25.

The diffusion of Ni into the *c*-axis-oriented Bi_2Te_3 was previously shown to result from solid-state reactions leading to the formation of Ni−Te bonds and formation of the topological AFM compound, $NiBi_2Te_4$.[25] Similar to that study, the room temperature $m(H)$ measurements can be used here as an indicator of the solid-state reaction of Ni with Bi_2Te_3 that is promoted by the delocalized TSS electrons. As shown in Figure 2h, all the Bi_2Te_3/Py samples show a clear decrease in the saturation magnetic moment for increasing disorder. This loss of saturation moment is compared to a control sample of Py by Δm. The $\Delta m\%$ values were found to be 13%, 37%, and 41% for the GBT, DBT, and CBT samples, respectively. This reduction in moments results from a change in valence state of the reacting magnetic species. Interestingly, in the samples with more highly disordered Bi_2Te_3, even though the diffusion of Ni is larger as observed in the EDS depth profiles in Figure 2d−f compared to the CBT/Py sample, the $\Delta m\%$ is lower. This clear enhancement in the loss of moments with crystalline order, and hence reactivity of Ni with Bi_2Te_3[25] is due to strengthening of TSS with increasing crystallinity of Bi_2Te_3. A lower number of the diffused magnetic species react and form compounds with Bi_2Te_3 due to weaker topological properties of highly disordered TI samples.

Disorder Effects on Room-Temperature Magnetic Properties of Bi_2Te_3/Py. To investigate the effects of disorder, $m(H)$ hysteresis loop and ferromagnetic resonance (FMR) experiments were performed on the three types of Bi_2Te_3 samples: highly disordered GBT/Py, moderately disordered DBT/Py, and *c*-axis-oriented CBT/Py. First, $m(H)$ hysteresis loop measurements were performed on the samples, with the magnetic field oriented in-plane (IP) and out-of-plane (OP) relative to the film plane, as shown in Figure 3a−c. For increasing *c*-axis-oriented growth of the Bi_2Te_3 layer, the saturation fields, H_s, measured in the IP and OP configurations show an increasing and decreasing trend,

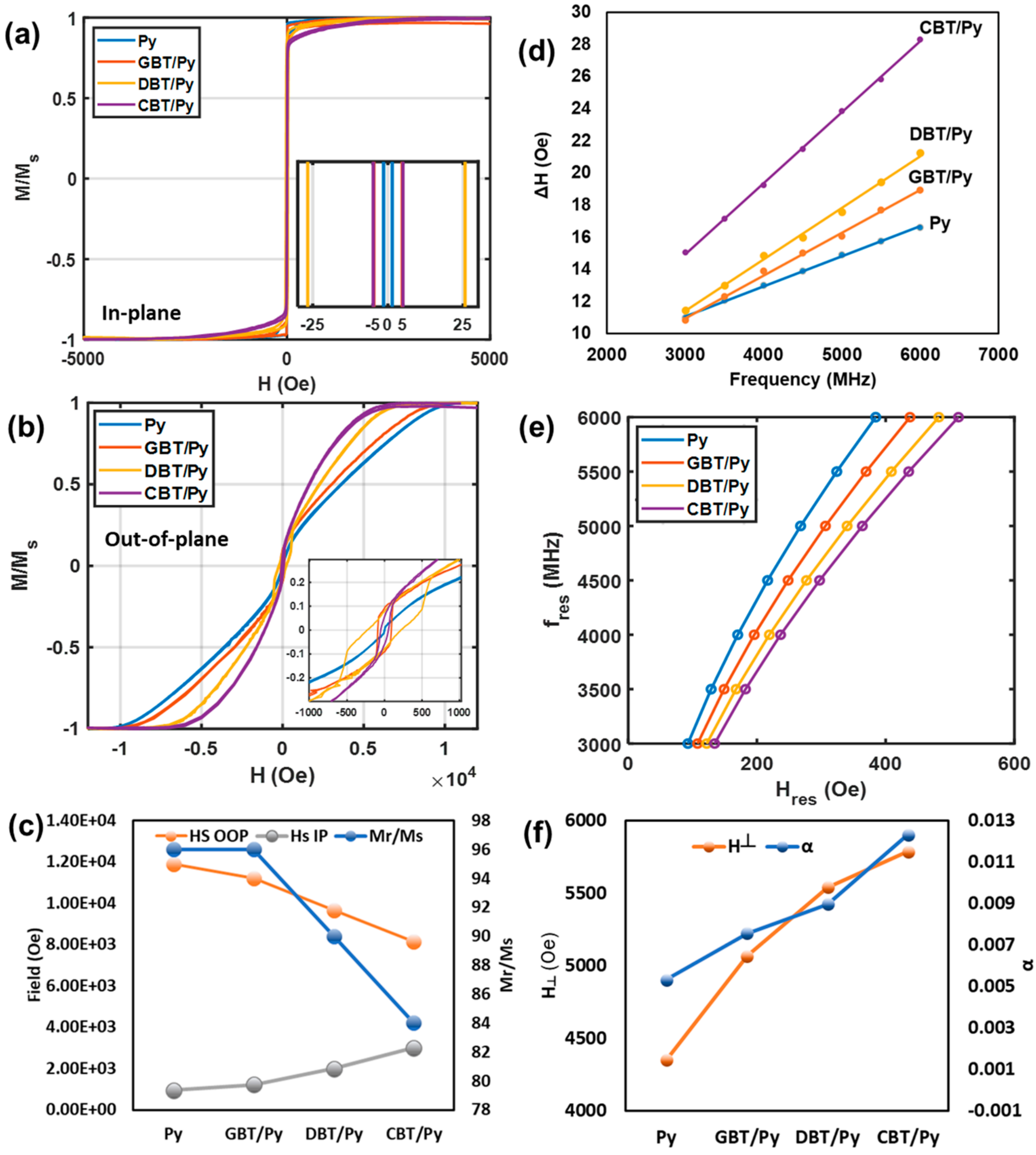

Figure 3. Normalized $m(H)$ loops measured (a) in-plane (normalized plots of Figure 2h) and (b) out-of-plane for the GBT/Py, DBT/Py, and CBT/Py samples. Inset: Expanded low-field regions showing enhanced H_c for the Bi_2Te_3/Py samples compared to the Py control sample. (c) Comparison of the saturation fields (IP and OP) and the M_r/M_s ratio clearly highlighting an increase in OP anisotropy with crystalline *c*-axis-orientation of Bi_2Te_3. (d) FMR line width versus frequency for extraction of α. (e) FMR resonance frequency versus field for extracting $H_\perp$ and $4\pi M_{eff}$. (f) Visual comparison of α and $H_\perp$ extracted from d and e, respectively. All measurements here were performed at 300 K.

respectively. In addition, the ratio of remanence to saturation magnetization (M_r/M_s) in the IP $m(H)$ loop decreases for increasing crystalline order of Bi_2Te_3. These trends indicate an increase in effective OP magnetic easy-axis with the increased *c*-axis-oriented texture of Bi_2Te_3 in the Bi_2Te_3/Py heterostructure samples. This enhanced OP magnetic anisotropy is a characteristic of interaction of the magnetic moments with large SOC in the interfaces.[31] Change in magnetic anisotropy has been previously predicted and observed in other TI/FM-based materials systems[32,33] (also see Supporting Information Section S6). As shown in Figure 3b, the OP measured $m(H)$ loops for the Bi_2Te_3/Py samples also exhibit a smaller hysteresis loop in the low-field regions. These smaller components of the $m(H)$ loop are more prominent in the DBT/Py and CBT/Py samples, which otherwise exhibit a lower OP easy-axis of magnetic moments compared to the highly *c*-axis-oriented CBT/Py sample. The DBT/Py sample also had an unusually large coercive field (H_c) resulting from the randomly oriented vdW layered crystalline domains, as observed in both the IP and OP $m(H)$ loop measurements in Figure 3a,b. These effects in the samples with highly disordered polycrystalline TIs are possibly present due to the disordered magnetic texture that emerge in their interfaces. Further, interfacial magnetic exchange interactions exist between the FM and Py layer and the diffused magnetic species in the randomly oriented vdW crystallite domains of the DBT sample. The randomly oriented vdW domains of the DBT sample may also have significant localized variations in

TSSs. A combination of these effects possibly lead to an anomalously large coercive field in the DBT/Py samples even at 300 K.

Further information was obtained using ferromagnetic resonance (FMR) measurements to understand the changes in magnetization *dynamics* with changes in TI disorder. The FMR line width (ΔH) and resonance field (H_{res}) were extracted from the FMR signal at different constant frequencies (f_{res}) (Supporting Information Section S4). The Gilbert damping parameter (α) was extracted by fitting a straight line to the FMR line width versus frequency plot using the equation, $\Delta H = \Delta H_0 + \frac{2\pi}{\gamma}\alpha f_{\mathrm{res}}$. Here, ΔH_0 is the inhomogeneous line width and γ is the gyromagnetic ratio. As shown in Figure 3d, the values of α extracted for the Py, GBT/Py, DBT/Py, and CBT/Py samples are 0.0053, 0.0076, 0.0089, and 0.0123, respectively. This shows a progressive increase in α with increase in crystallite grain size of Bi_2Te_3, and a significant enhancement when the Bi_2Te_3 layer is highly *c*-axis-oriented (summarized in Figure 3f). This effect was also observed in other Bi_2Te_3/FM heterostructure materials (Supporting Information Section S6), which signals a large enhancement in SOC and the presence of robust TSS in *c*-axis-oriented Bi_2Te_3. In addition, the effective magnetization, $4\pi M_{\mathrm{eff}}$, and the perpendicular magnetic anisotropy (PMA) field, $H_\perp$, were extracted by fitting the modified Kittel equation to the f_{res} versus H_{res} plots shown in Figure 3e,f, $f_{\mathrm{res}} = \frac{\gamma}{2\pi}\sqrt{(H_{\mathrm{res}} + H_a)(H_{\mathrm{res}} + H_a + 4\pi M_{\mathrm{eff}})}$, where $4\pi M_{\mathrm{eff}} = 4\pi M_s - H_\perp$ and H_a is the uniaxial anisotropy field. The $4\pi M_s$ values were found to be 15.2, 14.7, 14.3, and 14.1 kOe, respectively, for Py, GBT/Py, DBT/Py, and CBT/Py samples. The decrease in $4\pi M_s$ for increasing crystalline order demonstrates the reduction in saturation magnetization due to interfacial diffusion of Ni and Fe from Py into Bi_2Te_3.[25] In addition, the $H_\perp$ values increased from 4.35, 5.07, 5.54, and 5.79 kOe, for the Py, GBT/Py, DBT/Py, and CBT/Py samples, respectively. This enhancement in $H_\perp$ supports the $m(H)$ results that show an increase in effective OP anisotropy with increasing *c*-axis-oriented texture of Bi_2Te_3. The magnetic properties measured using $m(H)$ loops and FMR are summarized in Table 1.

Table 1. Summary of Room-Temperature Magnetic Properties of the GBT/Py, DBT/Py, and CBT/Py Heterostructure Samples

Sample	H_s OOP (kOe)	H_s IP (kOe)	M_r/M_s (%)	$4\pi M_s$ (kOe)	$H_\perp$-FMR (kOe)	α
Py	11.9	0.95	96	1.52	4.35	0.0053
GBT/Py	11.2	1.22	96	1.47	5.07	0.0075
DBT/Py	9.7	2.01	90	1.43	5.54	0.0089
CBT/Py	8.1	3.05	84	1.41	5.78	0.0123

The enhancement in α for increasing *c*-axis texture of Bi_2Te_3 can be attributed to a large spin-pumping effect modeled by the spin-mixing conductance, $g_{\uparrow\downarrow} = \frac{4\pi M_s t_{\mathrm{FM}} \Delta\alpha}{\hbar\gamma}$ where t_{FM} is the thickness of the FM layer, $\Delta\alpha$ is the enhancement in Gilbert damping, and $\hbar$ is the reduced Planck's constant. The resulting $g_{\uparrow\downarrow}$ values increased with increasing crystalline *c*-axis-orientation of Bi_2Te_3 and were 2.10×10^{-18}, 2.38×10^{-18}, and 4.08×10^{-18} m^{-2} for the GBT/Py, DBT/Py, and CBT/Py samples, respectively. The $g_{\uparrow\downarrow}$ values were calculated assuming that the Gilbert damping enhancement in the Bi_2Te_3/Py samples is entirely due to spin-pumping. The loss of magnetization from interfacial diffusion of Ni from Py and spin-memory loss due to interfacial proximity-induced magnetization[13−19] may also play a role in the enhancement of α in Bi_2Te_3/Py samples. However, these contributions toward enhancement in α could not be isolated because of complexity of interfaces in these heterostructure materials systems. However, the large enhancement in α with highly *c*-axis-oriented TIs is also observed in other TI/FM materials systems,[27,33−37] including those which do not show interfacial diffusion (see Supporting Information Section S6.1). This suggests that for crystalline *c*-axis-oriented TIs, the TI/FM heterostructures experience a significant enhancement in spin-pumping predominantly from the presence of robust TSS. These results provide strong evidence of enhancement in SOC strength and topological properties in highly *c*-axis-oriented TI samples compared to disordered TIs.

Spin−Orbit Torque Properties of CBT/Py, DBT/Py, and GBT/Py Samples. The spin−orbit torque (SOT) characteristics were extracted from the symmetric and antisymmetric components of the fitted Lorentzian, as shown in Figure 4b−d, using the equations[43] $V_s = -\frac{I_{\mathrm{rf}}\gamma\cos\theta_H}{4}\frac{\mathrm{d}R}{\mathrm{d}\theta_H}\left[\tau_{\mathrm{DL}}\frac{1}{\Delta}F_{\mathrm{sym}}\right]$ and $V_A = -\frac{I_{\mathrm{rf}}\gamma\cos\theta_H}{4}\frac{\mathrm{d}R}{\mathrm{d}\theta_H}\tau_\perp\frac{\left(1 + \frac{\mu_0 M_{\mathrm{eff}}}{H_{\mathrm{ext}}}\right)^{1/2}}{\Delta_{\mathrm{freq}}}F_{\mathrm{asym}}]$. Here, I_{rf} is the RF current injected, θ_H is the in-plane angle of the external DC field relative to the injected RF current, $\frac{\mathrm{d}R}{\mathrm{d}\theta_H}$ is the derivative of the anisotropic magnetoresistance (AMR) relative to θ_H (Supporting Information Section S5), Δ is the line width in the frequency domain, τ_{DL} is the damping-like DL-SOT, $\tau_\perp$ includes a combination the Oersted field torque and the field-like SOT (FL-SOT), γ is the gyromagnetic ratio, μ_0 is the permeability of vacuum, and ΔH is the line width of the FMR signal. τ_{DL} corresponds to the symmetric component of the Lorentzian, while $\tau_\perp$ corresponds to the antisymmetric components of the Lorentzian function.[43] The DL-SOT was the largest in the CBT/Py sample with a value of 0.16 Oe, compared to 0.11 and 0.10 Oe in GBT/Py and DBT/Py, respectively, as shown in Figure 4e. The FL-torques must have a finite contribution from Oersted fields because of the large thickness (∼20 nm) of the FM layers. The resistivity values of the Bi_2Te_3 samples capped with AlO_x were 3.56×10^{-5} Ωm, 5.83×10^{-5} Ωm, and 2.45×10^{-5} Ωm, respectively, for the GBT, DBT, and CBT samples, respectively. The reduced resistivity in CBT can lead to a larger charge current and hence larger DL-SOT in the CBT/Py sample. However, the DL-SOT value in the CBT/Py sample is much larger than expected compared to the GBT/Py and DBT/Py samples and cannot be explained solely on the basis of Bi_2Te_3 resistivities. Further, the resistivity of the Bi_2Te_3 layers in the GBT/Py, CBT/Py, and DBT/Py samples must have been altered by the interfacial diffusion of Ni,Fe and formation of compounds. A combination of all these factors along with presence of robust TSSs possibly leads to an enhanced DL-SOT in the CBT/Py sample which is much larger than the GBT/Py and DBT/Py samples.

The spin-Hall conductivity, σ_{SH}, which measures the spin current, J_s, generated from electric field, and E across the STFMR device is given by $\sigma_{\mathrm{SH}} = \frac{J_s}{E} = \frac{\tau_{\mathrm{DL}} M_s t_{\mathrm{FM}}}{E}$. The average

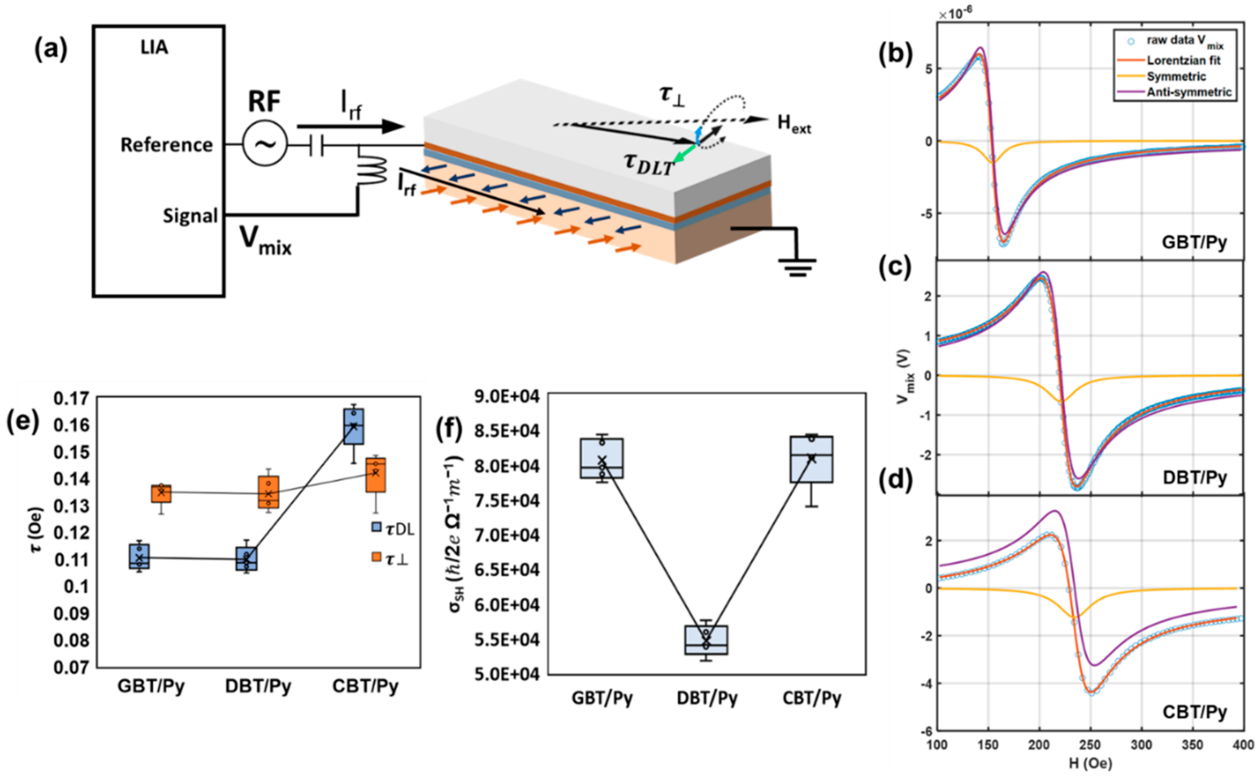

Figure 4. (a) Schematic for ST-FMR experimental setup with LIA and phase-locked RF current source. The brown and dark blue arrows signify up-spin and down-spin states, respectively. ST-FMR data and Lorentzian fitting for (b) GBT/Py, (c) DBT/Py, and (d) CBT/Py samples, measured at 4 GHz frequency. (e) DL-SOT (blue) and Oersted plus FL-SOT for the GBT/Py, CBT/Py, and DBT/Py samples extracted from b–d. (f) Values of σ_{SH} for the GBT/Py, CBT/Py, and DBT/Py samples. The boxes in (e) and (f) represent quartile plots for 5 devices in each sample measured.

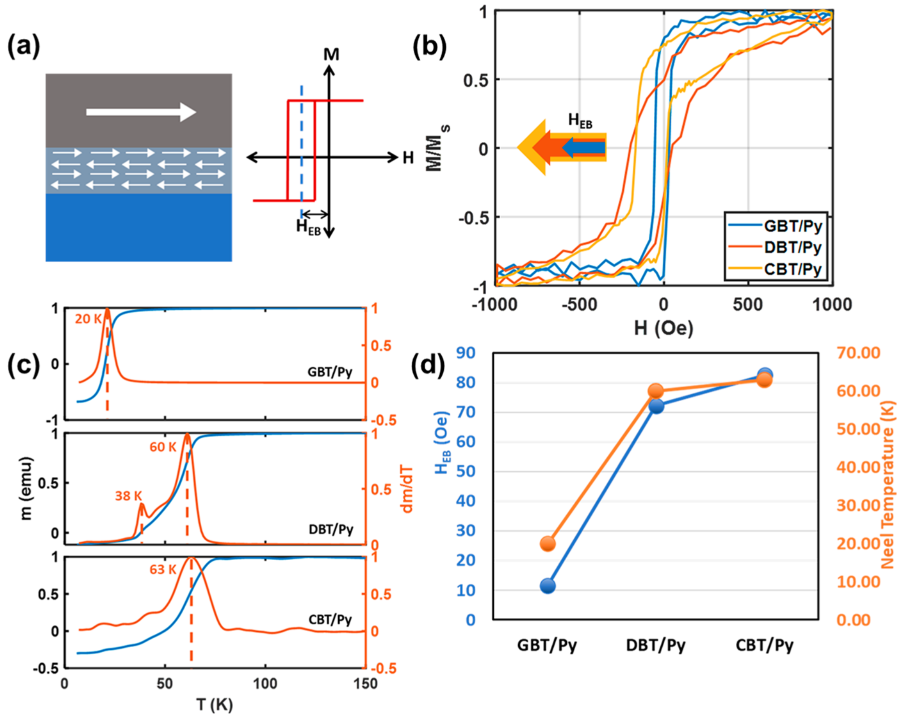

Figure 5. (a) Schematic of the AFM-FM heterostructure materials system and exchange bias in $m(H)$ loops. (b) $m(H)$ loops measured at 6 K under ZFC condition of the GBT/Py, DBT/Py, and CBT/Py[25] samples showing spontaneous exchange bias. The size of the arrows qualitatively indicates the magnitude of shifts in the exchange bias. (c) $m(T)$ measurements of the GBT/Py, DBT/Py, and CBT/Py samples and their derivatives for characterization of T_N. (d) Exchange bias and T_N values of the GBT/Py, DBT/Py, and CBT/Py samples extracted from b and c. The $m(H)$ and $m(T)$ data presented for the CBT sample are similar to the ones in ref 25.

https://doi.org/10.1021/acsaelm.2c00523
ACS Appl. Electron. Mater. 2022, 4, 4288−4297

σ_{SH} values shown in Figure 4f were calculated to be $8.1 \times 10^4 \frac{\hbar}{2e}$, $5.5 \times 10^4 \frac{\hbar}{2e}$, and $8.1 \times 10^4 \frac{\hbar}{2e} \Omega^{-1}\mathrm{m}^{-1}$ for GBT/Py, DBT/Py, and CBT/Py samples, respectively. The GBT/Py and CBT/Py samples have a much larger σ_{SH} compared to the disordered polycrystalline DBT/Py sample. This points toward a reduction in charge-spin current conversion efficiency with degradation in crystalline ordering possibly due to scattering of spin current in the randomly oriented crystalline TI domains. The GBT/Py sample, however, has a larger σ_{SH}, comparable to the DBT/Py sample and comparable to the CBT/Py sample. This happens possibly because of the quantum confinement effect in the smaller grain size of the GBT sample[26,27] resulting in larger charge-spin current conversion efficiency. The symmetric Lorentzian in ST-FMR also includes a contribution from spin-pumping due the inverse spin-Hall effect (ISHE), which results in the α enhancement due to spin-pumping, as shown in the Figure 3d. However, because of the complexity of the interface in the Bi_2Te_3/Py samples, ISHE contribution to the symmetric component of FMR spectra could not be accurately isolated from the DL-SOT. Further, the direct determination of spin-charge current interconversion efficiency requires determination of the spin-Hall angle, θ_{SH}, parameter.[43−45] Due to the complexity of the interfacial structure, the effective resistivity or the thickness of the spin-Hall material cannot be determined which are required for calculation of θ_{SH}. Hence, the spin-charge conversion efficiency for the Bi_2Te_3/Py samples could not be determined and compared accurately.

Effect of Crystalline Disorder in Interfacial Topological AFM Phase. Creation of an interfacial AFM-ordered layer was reported in the interface of highly *c*-axis-oriented Bi_2Te_3/Py heterostructures.[25] That AFM ordering in the interfacial layer was found to exist because of the presence of the topological AFM compound, $NiBi_2Te_4$. Here, the effect of crystalline disorder of Bi_2Te_3 on the AFM property of the Ni,Fe-diffused Bi_2Te_3 interface was also studied using zero-field-cooled (ZFC), $m(H)$, and $m(T)$ measurements at low temperatures as shown in Figure 5. Whereas the $m(H)$ measurements performed at 300 K are well-centered along the *H*-field axis, the $m(H)$ loops measured at 6 K shown in Figure 5b are significantly shifted off-center. This shift in the magnetic hysteresis loop is characteristic of spontaneous exchange bias that arises from an interfacial AFM−FM interaction given by $H_{EB} = \frac{J_{ex}}{4\pi M_s t_{FM}}$,[38−42] as illustrated in Figure 5a. Here, J_{ex} is the interfacial AFM−FM exchange energy and t_{FM} is the thickness of the ferromagnetic layer. As shown in Figures 4b,d, the CBT/Py with highly *c*-axis-oriented crystalline textured Bi_2Te_3 has the largest exchange bias of H_{EB} = 83 Oe, while the DBT/Py sample with randomly oriented polycrystalline grains of Bi_2Te_3 has a slightly reduced exchange bias of H_{EB} = 73 Oe. The exchange interaction strength in AFM materials is related to the Néel temperature, T_N which were determined using ZFC $m(T)$ measurements[39,41] at a constant field of 50 Oe, as shown in Figure 5c. The CBT/Py and DBT/Py samples also show high values of T_N = 63 and 60 K, respectively. It must also be noted that the large exchange bias and high T_N in the disordered DBT/Py sample should also have significant contributions from the larger Ni and Fe interface concentration of 46% and 9%, respectively, possibly causing the H_{EB} and T_N to be comparable to the highly *c*-axis-oriented CBT/Py sample. The DBT/Py sample also shows a secondary magnetic phase at T = 38 K also as observed from the smaller peak in the dm/dT plot in Figure 5c which can also influence the H_{EB} and H_c in the sample at measurement temperature of 6 K. This possibly emerges due to creation of an additional magnetic phase in the randomly oriented vdW crystalline domains affecting exchange interaction between the interfacial magnetic species. The highly disordered GBT/Py sample with granular Bi_2Te_3 had a large reduction in exchange bias to H_{EB} = 12 Oe and T_N = 20 K, clearly showing reduction in exchange interaction strength in the AFM interfacial layer. This follows from the much lower Δm and hence reduced reaction between the diffused Ni and Bi_2Te_3 in the GBT/Py sample compared to the DBT/Py and CBT/Py samples. In addition to the spontaneous exchange bias, the $m(H)$ measurements also show a characteristic enhancement in coercive field (H_c) in all the Bi_2Te_3/Py samples, as shown in Figure 5b, due to frustrated magnetic moments at the interface.[40] These results indicate the persistence of surface reactions and topological properties, even in highly disordered TIs.

CONCLUSION

Interfacial and magnetic properties of sputter-deposited TI/FM Bi_2Te_3/Py heterostructures were studied for three variations of the crystalline structural disorder of the Bi_2Te_3. An interface layer was found to form because of diffusion of Ni and smaller amounts of Fe into Bi_2Te_3. In conjunction with the experimental results reported in ref 25 a fraction of the diffused magnetic species was found to undergo solid-state chemical reactions with Bi_2Te_3 promoted by the TSS electrons. With the increasingly crystalline *c*-axis-oriented texture of Bi_2Te_3, strengthening the topological property of Bi_2Te_3 led to an enhancement in reaction between the diffused species and Bi_2Te_3. This was revealed by a larger loss of magnetic moments in higher *c*-axis-oriented Bi_2Te_3/Py heterostructures. The increase in crystalline *c*-axis-orientation of Bi_2Te_3 also resulted in a notable increase in OP magnetic anisotropy, Gilbert damping, and DL-SOT as observed from the $m(H)$ loop and FMR measurements. Interestingly, polycrystalline disordered Bi_2Te_3 sample had a reduced spin-Hall conductivity possibly because of scattering of spins from polycrystalline grain boundaries, whereas the samples with granular and highly *c*-axis-oriented Bi_2Te_3 had comparable charge-Hall conductivities, which possibly resulted from quantum confinement effect in smaller crystalline grains and strong TSS, respectively. Furthermore, magnetization measurements at low temperatures revealed a spontaneous exchange bias in all the Bi_2Te_3/Py heterostructures including the samples with highly disordered Bi_2Te_3. This further corroborated the evidence for interfacial solid-state reactions and demonstrated a surprising resilience of the topological property of disordered Bi_2Te_3. However, the exchange interaction strength of the interfacial AFM phase was found to weaken significantly with the increase in structural disorder of Bi_2Te_3. This was verified by degradation in H_{EB} and T_N with increase in disorder of the Bi_2Te_3. The weakened AFM exchange interaction and reduced magnetic moment loss suggested weakening of the topological property with an increase in the crystalline disorder of TI. These results will open the path for further exploration of the crystalline disorder in TIs and TI/FM interfaces and integration of TIs in practical spintronic devices.

EXPERIMENTAL SECTION

Material Growth. Bi_2Te_3 thin films of thickness ∼30 nm of varying crystalline disorder were grown by cosputtering a composite Bi_2Te_3 target with a Te target, using RF magnetron sputtering at 90 and 20 W, respectively, with 4 mTorr Ar pressure on thermally oxidized Si substrates. The base pressure of the sputtering chamber was $\sim 8 \times 10^{-8}$ Torr. The GBT, DBT, and CBT samples were grown with substrate maintained at 20, 160, and 250 °C, respectively. The DBT and CBT samples were further annealed at the growth temperatures inside the PVD process chamber in 45 mTorr pressure in Ar environment for 25 min. The CBT samples were grown using the same method as ref 25. The samples were capped with 2 nm Al at room temperature before breaking vacuum which oxidizes to AlO_x on exposure to atmosphere. For the magnetic and ST-FMR experiments, 20 nm Py and 3 nm TiO_x capping were deposited at room temperature after deposition of Bi_2Te_3. For the X-ray, TEM, and $m(H)$ hysteresis loop measurements, the same samples with precise dimensions of 5 × 6 mm^2 were used. Samples for STFMR measurements were deposited on 3 in. wafers.

XRD Characterization. X-ray diffraction was collected using a background-free, highly collimated beam of Cu−Kα1 radiation (wavelength λ = 1.54056 Å).[25] The X-rays were captured by a 2D charged-coupled device (CCD). The Bragg reflections were indexed according to the Bi_2Te_3 bulk hexagonal unit cell, as indicated by $(h, k, -(h + k), l)$ where h, k, and l are the Miller indices.[25]

TEM and XEDS Characterization. Samples for TEM investigations were prepared by focused ion beam milling (FIB) using a Ga^+ ion source. Prior to TEM observation, an additional cleaning procedure was performed by Ar-ion milling to reduce a surface amorphous layer and residual Ga from the FIB process. The TEM observations were performed using a Talos 200-FX (ThermoFiszher Scientific Inc.) TEM operated at an acceleration voltage of 200 kV.[25] EDS measurements were performed using a ChemiSTEM (Thermo-Fisher Scientific), and processing of the spectra was performed using Esprit 1.9 (Bruker Inc.) software.[25]

FMR Measurements. FMR measurements of α, $4\pi M_{\text{eff}}$, and H_a were performed using a spin-torque FMR (ST-FMR) experimental setup. The analysis of the experiment is explained in Supporting Information Section S4. RF current is provided by a HP8350 RF source. A SR830 lock-in amplified (LIA) provides reference low-frequency AC for modulation phase-locked with the RF current. The LIA was used for detection of ST-FMR signal. The bias DC field is provided by an Fe-core electromagnet on a rotating stage with precise angular control. The reported ST-FMR experiment was performed at a 45° angle of the microstrip relative to the DC bias field. Control of the experiment and data acquisition were done using NI LabVIEW. The S11, S12, and impedance values were used to calculate the RF current and the E-field using vector network analyzer (VNA). The total power lost in the electrical components, such as wires and connectors, was measured to be ∼60%; hence, 40% of 8 dbm power was used for RF current calculations. FMR characteristics in the Bi_2Te_3/Py heterostructure samples were also extracted from the ST-FMR experiment spectra as shown in Figure S2. The devices were patterned using an ion-milling process for the DBT/Py and CBT/Py samples and using a lift-off process for the Py and GBT/Py samples. The FMR characteristics were extracted by fitting Lorentzian functions to the spectra,[43] as shown in Figure S2a−d, using the equation, $V_{\text{mix}} = V_S F_{\text{sym}} + V_A F_{\text{asym}}$, which clearly shows broadening of the FMR line width progressively from Py, GBT/Py, and DBT/Py to CBT/Py samples. Here, V_{mix} is the DC voltage output recorded in the LIA, $F_{\text{sym}} = \frac{\Delta H^2}{(\mu_0 H - \mu_0 H_{\text{res}})^2 + \Delta H^2}$ and $F_{\text{asym}} = \frac{\Delta H(\mu_0 H - \mu_0 H_{\text{FMR}})}{(\mu_0 H - \mu_0 H_{\text{res}})^2 + \Delta H^2}$ are the symmetric and antisymmetric components of the Lorentzian function, ΔH is the line width of the FMR signal, and H_{res} is the FMR field. The ST-FMR measurements were performed at a 45° angle relative to the external applied magnetic field. The values of ΔH, H_{FMR}, V_S, and V_A were extracted by fitting the ST-FMR signal using the equation above for the analysis of α, $4\pi M_s$, $H_\perp$, and θ_{SH} reported in the main text.[25]

Hysteresis Loop Measurements. Magnetization $m(H)$ and $m(T)$ measurements were obtained using a Quantum Design MPMS XL-7 superconducting quantum interference device (SQUID) magnetometer.[25] Hysteresis loop $m(H)$ measurements were carried out at various temperatures between 6 and 300 K. The ZFC $m(T)$ measurements were obtained while increasing the temperature in an applied field of 50 Oe. Room temperature $m(H)$ measurements were taken using a vibrating sample magnetometer (VSM).

ASSOCIATED CONTENT

Supporting Information

The Supporting Information is available free of charge at https://pubs.acs.org/doi/10.1021/acsaelm.2c00523.

Additional experimental data with figures (PDF)

AUTHOR INFORMATION

Corresponding Author

Nian Xiang Sun − *Northeastern University, Department of Electrical and Computer Engineering, Boston, Massachusetts 02115, United States;* orcid.org/0000-0002-3120-0094; Email: n.sun@northeastern.edu

Authors

Nirjhar Bhattacharjee − *Northeastern University, Department of Electrical and Computer Engineering, Boston, Massachusetts 02115, United States*

Krishnamurthy Mahalingam − *Air Force Research Laboratory, Nano-electronic Materials Branch, Wright Patterson Air Force Base, Ohio 05433, United States*

Adrian Fedorko − *Northeastern University, Department of Physics, Boston, Massachusetts 02115, United States*

Alexandria Will-Cole − *Northeastern University, Department of Electrical and Computer Engineering, Boston, Massachusetts 02115, United States*

Jaehyeon Ryu − *Northeastern University, Department of Electrical and Computer Engineering, Boston, Massachusetts 02115, United States*

Michael Page − *Air Force Research Laboratory, Nano-electronic Materials Branch, Wright Patterson Air Force Base, Ohio 05433, United States*

Michael McConney − *Air Force Research Laboratory, Nano-electronic Materials Branch, Wright Patterson Air Force Base, Ohio 05433, United States*

Hui Fang − *Northeastern University, Department of Electrical and Computer Engineering, Boston, Massachusetts 02115, United States;* Present Address: Dartmouth College, Thayer School of Engineering, Hanover, NH 03755

Don Heiman − *Northeastern University, Department of Physics, Boston, Massachusetts 02115, United States; Plasma Science and Fusion Center, MIT, Cambridge, Massachusetts 02139, United States*

Complete contact information is available at: https://pubs.acs.org/10.1021/acsaelm.2c00523

Author Contributions

The manuscript was written through contributions of all authors. All authors have given approval to the final version of the manuscript.

Funding

This work is partially supported by the U.S Army under grant no. W911NF20P0009, the NIH Award UF1NS107694, and the NSF TANMS ERC Award 1160504. The work of DH and AF was partially supported by the National Science

Foundation grant DMR-1905662 and the Air Force Office of Scientific Research award FA9550-20-1-0247. The work of KM was supported by Air Force Research Laboratory under AFRL/NEMO contract: FA8650-19-F-5403 TO3. Studies employing the Titan 60-300 TEM was performed at the Center for Electron Microscopy and Analysis (CEMAS) at The Ohio State University with support through Air Force contract FA8650-18-2-5295.

Notes

The authors declare no competing financial interest.

■ ACKNOWLEDGMENTS

We thank Charles Settens and MIT, Materials Research Laboratory for their help with XRD measurements. We thank Neville Sun and Mehdi Nasrollahpourmotlaghzanjani for help with VNA measurements. We also thank Ivan Lisenkov for his valuable input in understanding FMR experiments. Certain commercial equipment is identified in this paper to foster understanding, but such identification does not imply recommendation or endorsement by Northeastern University and AFRL.

■ ABBREVIATIONS

AFM, Antiferromagnet; CBT, *c*-axis-oriented Bi_2Te_3; DBT, Disordered Bi_2Te_3; DL-SOT, Damping-like spin orbit torque; EDS, Energy-dispersive X-ray spectroscopy; FM, Ferromagnet; FMR, Ferromagnetic resonance; GBT, Granular Bi_2Te_3; HRTEM, High resolution transmission electron microscopy; IP, In-plane; MBE, Molecular beam epitaxy; OP, Out-of-plane; QAH, Quantum anomalous hall; RF, Radiofrequency; SOC, Spin orbit coupling; TI, Topological insulator; TSS, Topological surface states; XRD, X-ray diffraction; XRR, X-ray reflectometry; ZFC, Zero field cooled.

■ REFERENCES

(1) Zhang, H.; Liu, C. X.; Qi, X. L.; Dai, X.; Fang, Z.; Zhang, S. C. Topological insulators in Bi_2Se_3, Bi_2Te_3 and Sb_2Te_3 with a single Dirac cone on the surface. *Nat. Phys.* **2009**, *5*, 438−442.

(2) Chen, Y. L.; Analytis, J. G.; Chu, J.-H.; Liu, Z. K.; Mo, S.-K.; Qi, X. L.; Zhang, H. J.; Lu, D. H.; Dai, X.; Fang, Z.; Zhang, S. C.; Fisher, I. R.; Hussain, Z.; Shen, Z. X. Experimental Realization of a Three-Dimensional Topological Insulator, Bi_2Te_3. *Science* **2009**, *325*, 178.

(3) Zhang, Y.; He, K.; Chang, C. Z.; Song, C. L.; Wang, L. L.; Chen, X.; Jia, J. F.; Fang, Z.; Dai, X.; Shan, W. Y.; Shen, S. Q.; Niu, Q.; Qi, X. L.; Zhang, S. C.; Ma, X. C.; Xue, Q. K. Crossover of the three-dimensional topological insulator Bi_2Se_3 to the two-dimensional limit. *Nat. Phys.* **2010**, *6*, 584−588.

(4) Yu, R.; Zhang, W.; Zhang, H. J.; Zhang, S. C.; Dai, X.; Fang, Z. Quantized anomalous Hall effect in magnetic topological insulators. *Science* **2010**, *329*, 61−64.

(5) Chang, C. Z.; Zhang, J.; Feng, X.; Shen, J.; Zhang, Z.; Guo, M.; Li, K.; Ou, Y.; Wei, P.; Wang, L. L.; Ji, Z. Q.; Feng, Y.; Ji, S.; Chen, X.; Jia, J.; Dai, X.; Fang, Z.; Zhang, S. C.; He, K.; Wang, Y.; Lu, L.; Ma, X. C.; Xue, Q. K. Experimental observation of the quantum anomalous Hall effect in a magnetic topological insulator. *Science* **2013**, *340*, 167−170.

(6) Chang, C. Z.; Zhao, W.; Kim, D. Y.; Zhang, H.; Assaf, B. A.; Heiman, D.; Zhang, S. C.; Liu, C.; Chan, M. H.; Moodera, J. S. High-precision realization of robust quantum anomalous Hall state in a hard ferromagnetic topological insulator. *Nat. Mater.* **2015**, *14*, 473−477.

(7) Tokura, Y.; Yasuda, K.; Tsukazaki, A. Magnetic Topological Insulators. *Nat. Rev. Phys.* **2019**, *1*, 126−143.

(8) Liu, C.; Wang, Y.; Li, H.; Wu, Y.; Li, Y.; Li, J.; He, K.; Xu, Y.; Zhang, J.; Wang, Y. Robust axion insulator and Chern insulator phases in a two-dimensional antiferromagnetic topological insulator. *Nat. Mater.* **2020**, *19*, 522−527.

(9) Wang, W.; Ou, Y.; Liu, C.; Wang, Y.; He, K.; Xue, Q. K.; Wu, W. Direct evidence of ferromagnetism in a quantum anomalous Hall system. *Nat. Phys.* **2018**, *14*, 791−795.

(10) Teng, J.; Liu, N.; Li, Y. Mn-doped topological insulators: a review. *J. Semicond.* **2019**, *40*, No. 081507.

(11) Tcakaev, A.; Zabolotnyy, V. B.; Fornari, C. I.; Rußmann, P.; Peixoto, T. R. F.; Stier, F.; Dettbarn, M.; Kagerer, P.; Weschke, E.; Schierle, E.; Bencok, P.; Rappl, P. H. O.; Abramof, E.; Bentmann, H.; Goering, E.; Reinert, F.; Hinkov, V. Incipient antiferromagnetism in the Eu-doped topological insulator Bi_2Te_3. *Phys. Rev. B* **2020**, *102*, 184401.

(12) Ni, Y.; Zhang, Z.; Nlebedim, I. C.; Hadimani, R. L.; Tuttle, G.; Jiles, D. C. Ferromagnetism of magnetically doped topological insulators in Cr_xBi_2_xTe_3 thin films. *J. Appl. Phys.* **2015**, *117*, 17C748.

(13) Katmis, F.; Lauter, V.; Nogueira, F. S.; Assaf, B. A.; Jamer, M. E.; Wei, P.; Satpati, B.; Freeland, J. W.; Eremin, I.; Heiman, D.; Jarillo-Herrero, P.; Moodera, J. S. A high-temperature ferromagnetic topological insulating phase by proximity coupling. *Nat.* **2016**, *533*, 513−516.

(14) Che, X.; Murata, K.; Pan, L.; He, Q. L.; Yu, G.; Shao, Q.; Yin, G.; Deng, P.; Fan, Y.; Ma, B.; Liang, X.; Zhang, B.; Han, X.; Bi, L.; Yang, Q. H.; Zhang, H.; Wang, K. L. Proximity-Induced Magnetic Order in a Transferred Topological Insulator Thin Film on a Magnetic Insulator. *ACS Nano* **2018**, *12*, 5042−5050.

(15) Lee, C.; Katmis, F.; Jarillo-Herrero, P.; Moodera, J. S.; Gedik, N. Direct measurement of proximity-induced magnetism at the interface between a topological insulator and a ferromagnet. *Nat. Commun.* **2016**, *7*, 12014.

(16) Choi, W. Y.; Jeon, J. H.; Bang, H. W.; Yoo, W.; Jerng, S. K.; Chun, S. H.; Lee, S.; Jung, M. H. Proximity-Induced Magnetism Enhancement Emerged in Chiral Magnet MnSi/Topological Insulator Bi_2Se_3 Bilayer. *Adv. Quant. Technol.* **2021**, *4*, 2000124.

(17) Hutasoit, J. A.; Stanescu, T. D. Induced spin texture in semiconductor/topological insulator heterostructures. *Phys. Rev. B* **2011**, *84*, No. 085103.

(18) Marmolejo-Tejada, J. M.; Dolui, K.; Lazic, P.; Chang, P. H.; Smidstrup, S.; Stradi, D.; Stokbro, K.; Nikolic, B. K. Proximity Band Structure and Spin Textures on Both Sides of Topological Insulator/Ferromagnetic-Metal Interface and Their Charge Transport Probes. *Nano Lett.* **2017**, *17*, 5626−5633.

(19) Zutic, I.; Matos-Abiague, A.; Scharf, B.; Dery, H.; Belashchenko, K. Proximitized Materials. *Mater. Today* **2019**, *22*, 85.

(20) Li, J.; Li, Y.; Du, S.; Wang, Z.; Gu, B. L.; Zhang, S. C.; He, K.; Duan, W.; Xu, Y. Intrinsic magnetic topological insulators in van der Waals layered $MnBi_2Te_4$-family materials. *Sci. Adv.* **2019**, *5*, eaaw5685.

(21) Li, Z.; Li, J.; He, K.; Wan, X.; Duan, W.; Xu, Y. Tunable interlayer magnetism and band topology in van derWaals heterostructures of $MnBi_2Te_4$-family materials. *Phys. Rev. B* **2020**, *102*, 081107.

(22) Walsh, L. A.; Smyth, C. M.; Barton, A. T.; Wang, Q.; Che, Z.; Yue, R.; Kim, J.; Kim, M. J.; Wallace, R. M.; Hinkle, C. L. Interface Chemistry of Contact Metals and Ferromagnets on the Topological Insulator Bi2Se3. *J. Phys. Chem. C* **2017**, *121*, 23551−23563.

(23) Ferfolja, K.; Fanetti, M.; Gardonio, S.; Panighel, M.; Pis, I.; Nappini, S.; Valant, M. A cryogenic solid-state reaction at the interface between Ti and the Bi_2Se_3 topological insulator. *J. Mater. Chem. C* **2020**, *8*, 11492−11498.

(24) Li, G.; Felser, C. Heterogeneous catalysis at the surface of topological materials. *Appl. Phys. Lett.* **2020**, *116*, No. 070501.

(25) Bhattacharjee, N.; Mahalingam, K.; Fedorko, A.; Lauter, V.; Matzelle, M.; Singh, B.; Grutter, A.; Will-Cole, A.; Page, M.; McConney, M.; Markiewicz, R.; Bansil, A.; Heiman, D.; Sun, N. X. Topological Antiferromagnetic Van der Waals Phase in Topological Insulator/Ferromagnet Heterostructures Synthesized by a CMOS-Compatible Sputtering Technique. *Adv. Mater.* **2022**, *34*, 1.

(26) DC, M.; Grassi, R.; Chen, J.-Y.; Jamali, M.; Reifsnyder Hickey, D.; Zhang, D.; Zhao, Z.; Li, H.; Quarterman, P.; Lv, Y.; Li, M.; Manchon, A.; Mkhoyan, K. A.; Low, T.; Wang, J.-P. Room-temperature high spin-orbit torque due to quantum confinement in sputtered $Bi_xSe_{(1-x)}$ films. *Nat. Mater.* **2018**, *17*, 800.

(27) DC, M.; Liu, T.; Chen, J. Y.; Peterson, T.; Sahu, P.; Li, H.; Zhao, Z.; Wu, M.; Wang, J. P. Room-temperature spin-to-charge conversion in sputtered bismuth selenide thin films via spin pumping from yttrium iron garnet. *Appl. Phys. Lett.* **2019**, *114*, 102401.

(28) Guo, Q.; Wu, Y.; Xu, L.; Gong, Y.; Ou, Y.; Liu, Y.; Li, L.; Yan, Y.; Han, G.; Wang, D.; Wang, L.; Long, S.; Zhang, B.; Cao, X.; Yang, S.; Wang, X.; Huang, Y.; Liu, T.; Yu, G.; He, K.; Teng, J. Electrically Tunable Wafer-Sized Three-Dimensional Topological Insulator Thin Films Grown by Magnetron Sputtering. *Chin. Phys. Lett.* **2020**, *37*, No. 057301.

(29) Guo, Q. X.; Ren, Z. X.; Huang, Y. Y.; Zheng, Z. C.; Wang, X. M.; He, W.; Zhu, Z. D.; Teng, J. Effects of post-annealing on crystalline and transport properties of Bi_2Te_3 thin films. *Chin. Phys. B* **2021**, *30* (6), No. 067307.

(30) Corbae, P.; Ciocys, S.; Varjas, D.; Kennedy, E.; Zeltmann, S.; Molina-Ruiz, M.; Griffin, S.; Jozwiak, C.; Chen, Z.; Wang, L. W.; Minor, A. M.; Scott, M.; Grushin, A. G.; Lanzara, A.; Hellman, F. Evidence for topological surface states in amorphous Bi_2Se_3. *arXiv* [cond-mat.mtrl-sci], 2021, 1910.13412.

(31) Yi, D.; Liu, J.; Hsu, S. L.; Zhang, L.; Choi, Y.; Kim, J. W.; Chen, Z.; Clarkson, J. D.; Serrao, C. R.; Arenholz, E.; Ryan, P. J.; Xu, H.; Birgeneau, R. J.; Ramesh, R. Atomic-scale control of magnetic anisotropy via novel spin−orbit coupling effect in $La_{2/3}Sr_{1/3}MnO_3/SrIrO_3$ superlattices. *Proc. Natl. Acad. Sci. U.S.A.* **2016**, *113* (23), 6397.

(32) Semenov, Y. G.; Duan, X.; Kim, K. W. Electrically controlled magnetization in ferromagnet-topological insulator heterostructures. *Phys. Rev. B* **2012**, *86*, 161406.

(33) Liu, T.; Kally, J.; Pillsbury, T.; Liu, C.; Chang, H.; Ding, J.; Cheng, Y.; Hilse, M.; Engel-Herbert, R.; Richardella, A.; Samarth, N.; Wu, M. Changes of Magnetism in a Magnetic Insulator due to Proximity to a Topological Insulator. *Phys. Rev. Lett.* **2020**, *125*, No. 017204.

(34) Jamali, M.; Lee, J. S.; Jeong, J. S.; Mahfouzi, F.; Lv, Y.; Zhao, Z.; Nikolić, B. K.; Mkhoyan, K. A.; Samarth, N.; Wang, J. P. Significant Spin Pumping and Inverse Spin Hall Effect in the Presence of Surface and Bulk Spin−Orbit Coupling of Topological Insulator Bi_2Se_3. *Nano Lett.* **2015**, *15* (10), 7126.

(35) Wang, H.; Kally, J.; Şahin, C.; Liu, T.; Yanez, W.; Kamp, E. J.; Richardella, A.; Wu, M.; Flatté, M. E.; Samarth, N. Fermi level dependent spin pumping from a magnetic insulator into a topological insulator. *Phys. Rev. Res.* **2019**, *1*, No. 012014.

(36) Hou, Y. S.; Wu, R. Q. Strongly Enhanced Gilbert Damping in 3d Transition-Metal Ferromagnet Monolayers in Contact with the Topological Insulator Bi_2Se_3. *Phys. Rev. Appl.* **2019**, *11*, No. 054032.

(37) Chiba, T.; Leon, A. O.; Komine, T. Voltage-control of damping constant in magnetic-insulator/topological-insulator bilayers. *Appl. Phys. Lett.* **2021**, *118*, 252402.

(38) Li, M.; Chang, C. Z.; Kirby, B. J.; Jamer, M. E.; Cui, W.; Wu, L.; Wei, P.; Zhu, Y.; Heiman, D.; Li, J.; Moodera, J. S. Proximity-Driven Enhanced Magnetic Order at Ferromagnetic-Insulator−Magnetic-Topological-Insulator Interface. *Phys. Rev. Lett.* **2015**, *115*, No. 087201.

(39) Murthy, J. K.; Anil Kumar, P. S. Interface-induced spontaneous positive and conventional negative exchange bias effects in bilayer $La_{0.7}Sr_{0.3}MnO_3/Eu_{0.45}Sr_{0.55}MnO_3$ heterostructures. *Sci. Rep.* **2017**, *7*, 6919.

(40) Leighton, C.; Nogues, J.; Jonsson-Akerman, B. J.; Schuller, I. K. Coercivity Enhancement in Exchange Biased Systems Driven by Interfacial Magnetic Frustration. *Phys. Rev. Lett.* **2000**, *84*, 3466.

(41) Maity, T.; Goswami, S.; Bhattacharya, D.; Roy, S. Superspin Glass Mediated Significant Spontaneous Exchange Bias in a Nanocomposite of $BiFeO_3{-}Bi_2Fe_4O_9$. *Phys. Rev. Lett.* **2013**, *110*, 107201.

(42) Liu, J.; Singh, A.; Yang, Y.; Liu, F.; Ionescu, A.; Kuerbanjiang, B.; Barnes, C. H. W.; Hesjedal, T. Exchange Bias in Magnetic Topological Insulator Superlattices. *Nano Lett.* **2020**, *20*, 5315.

(43) Wang, Y.; Ramaswamy, R.; Yang, H. FMR-Related Phenomena in Spintronic Devices. *J. Phys. D: Appl. Phys.* **2018**, *51*, 273002.

(44) Kondou, K.; Sukegawa, H.; Kasai, S.; Mitani, S.; Niimi, Y.; Otani, Y. C. Influence of Inverse Spin Hall Effect in Spin-Torque Ferromagnetic Resonance Measurements. *Appl. Phys. Exp.* **2016**, *9*, No. 023002.

(45) Bonell, F.; Goto, M.; Sauthier, G.; Sierra, J. F.; Figueroa, A. I.; Costache, M. V.; Miwa, S.; Suzuki, Y.; Valenzuela, S. O. Control of Spin−Orbit Torques by Interface Engineering in Topological Insulator Heterostructures. *Nano Lett.* **2020**, *20* (8), 5893.